Engineering Applications of Computational Fluid Mechanics Vol. 7, No. 4, pp. 507–518 (2013)

MODELING PROPAGATION OF 2011 HONSHU TSUNAMI

Wenfang Lu *, Yuwu Jiang *† and Jian Lin **

* *State Key Laboratory of Marine Environmental Science, Xiamen University, Xiamen, 361005, Fujian, China*
† *E-Mail: ywjiang@xmu.edu.cn* (*Corresponding Author)*
** *Woods Hole Oceanographic Institution, Woods Hole, MA 02543-1050, USA*

ABSTRACT: In this study, the Honshu tsunami on 11 March 2011 was simulated using the Regional Ocean Model System (ROMS) governed by two-dimensional nonlinear shallow-water equations and driven by three earthquake deformation fields as initial condition. The purpose of this study is to assess the model's sensitivity to the tsunami source field, especially the case in which the horizontal deformation of earthquake was taken into account. The comparison between the model results and observed tsunami waves at 14 Deep-ocean Assessment and Reporting of Tsunami (DART) buoy stations showed that the average errors of modeled maximum wave amplitude were 23.2%, 26.9% and 37.4% for the three initial deformation fields, respectively. In the best performance case, when the observed wave amplitude was below 0.3 m, the average error of the modeled maximum wave amplitude was 0.034 m and relative error was 23.7%. On the other hand, the average errors of modeled arrival times of the first tsunami-wave peak at 13 DART stations were 2.82, 2.28 and 3.48 min earlier for the three cases of different initial fields, but the error is as big as ~3 hrs at Station 46412 located near the west coast of the USA. The model did not resolve the observed wave at Station 46412, which might be caused by the model's coarse grid that cannot represent the bottom topography well, especially that near the shoreline. The two-dimensional (2D) model employing shallow-water equations could also be a limiting factor. In Case 4 based on the best performance case with horizontally generated wave, the average relative error of maximum wave amplitude was reduced from 23.2% to 20.6% and the root mean square error (RMSE) was reduced from 0.029 m to 0.014 m. The results suggest that the consideration of horizontal deformation of earthquake, which plays an important role in generating tsunami, can help to improve the performance of simulating tsunami wave.

Keywords: Japan earthquake; tsunami; numerical simulation; deformation field

1. INTRODUCTION

On 11 March 2011, an earthquake of magnitude M_w=9.0 occurred to the east of Honshu in Japan, causing a great tsunami disaster. The tsunami killed over 15,000 people and resulted in thousands of people missing. Since 1993, Japan has been building a tsunami warning system based on finite fault model and pre-computed tsunami-wave database. The numerical model plays an important role in both tsunami research and warning. After the massive tsunami in 2011, several simulation efforts were made among the tsunami modeling community. Yamazaki et al. (2012) validated a nested-grid model with the near-shore observatory in Honolulu, Hawaii, and concluded that a hydrodynamic model is able to shade light on the inherent processes of tsunami waves. Chen et al. (2012) tested five seismic rupture models as the initial conditions with a high-resolution, nested Finite-Volume Community Ocean Model (FVCOM) system, providing an alternative way to evaluate the seismic model, i.e., from the relative performance when driving hydrodynamic models.

In terms of tsunami forecasting, the NOAA's methodology is a system combining seismic and direct real-time deep ocean tsunami measurements for coastal predictions, while the Japan Meteorological Agency's (JMA's) system is based primarily on indirect tsunami measurements, seismic and GPS data (Tang et al., 2009). Although operational tsunami warning system based on numerical simulation has been built up, tsunami wave simulation based on Okada's earthquake source parameters model (Okada, 1985) is not yet accurate enough (Wen et al., 2011). However, the limitations of the system, resulting from the limitations of our knowledge on the under-seabed seismic processes, had never been highlighted until the Honshu tsunami occurred. The underestimated tsunami wave height in Honshu tsunami resulting in great damage indicates that much work still needs to be done in terms of tsunami simulation (Avouac et al., 2011).

Received: 14 Mar. 2013; Revised: 7 Jul. 2013; Accepted: 12 Aug. 2013

A tsunami commonly has three stages, i.e., generation, propagation and inundation. In the generation stage, Okada's finite fault deformation model is widely used as the initial method to predict the initial sea surface displacement of a tsunami (Okada, 1985). This method assumes that an earthquake can be regarded as the rupture of a single fault plane. This fault is described by a series of parameters, comprising dip angle, strike angle, rake angle, fault width, fault length, and fault depth. Okada's vertical displacement is applied to generate tsunami wave with initialized sea-surface elevation instantaneously (e.g., Satake 1995), or drive the model at a specific rupture time (e.g., Yamazaki et al., 2012). The former application is likely to underestimate tsunami wave height because the earthquake energy release is a sustained process, instead of an instant process (Wen et al., 2011). The sensitive tests, focused on seismic rupture parameters, are reliable approaches to improve the simulation performance, because they can evaluate the initial condition for the models (Yamazaki et al., 2011). Recently, tsunami-wave generations independent of the Okada's assumption are also developed and evaluated, in which a 3D Finite Element Model is employed (Grilli et al., 2012). In the propagation stage, two main types of governing equations had been employed in previous research, the Boussinesq equations (Chawla and Kirby, 2000; Tappin et al., 2001; Zhang et al., 2010), or the nonlinear shallow-water equations (Kilinc et al., 2009; Tang et al., 2009; Kowalik and Proshutinsky, 2010; Olabarrieta et al., 2010). Results have shown that the dispersive effects, which are excluded from the shallow-water equations used in this study, are not significant for the type of tsunami source in the 2011 Honshu earthquake (Grilli et al., 2012). In the inundation stage, two-way nested models are frequently employed since they are of high efficiency and precision when resolving the near-shore processes (e.g., Tang et al., 2009; Chen et al., 2012). Precise simulation of the inherent processes over the shelf interacted with the topography would be useful in hazard assessment and tsunami warning (Yamazaki et al., 2012).

In this study, the tsunami wave is driven by the instantaneous sea surface disturbance derived from Okada's finite fault model and the propagation stage of tsunami is simulated with the use of nonlinear shallow-water equations. Four cases are considered with three different earthquake deformation fields. In Cases 1 to 3, only vertical deformation is considered. In Case 4, we modify the genesis method, i.e., the effect of the horizontal deformation of earthquake is taken into account based on Case 1. The basic information of the four cases is presented in Section 2, as well as the model description, method and validation data. Even with the availability of numerous seismic data, how the rupture process affects the tsunami genesis is still unclear, due to the lack of an adequate theory to use the data for tsunami hazard assessment (Avouac et al., 2011). To facilitate theoretical progress in tsunami simulation, we mainly focus on the comparison of the modeled and observed tsunami waves to evaluate the three earthquake deformation fields from different deformation sources. The goal is to understand how the output from a tsunami source model, i.e., Okada's finite fault model, can affect the results from a hydrodynamic model, i.e., the Regional Ocean Modeling System (ROMS) used in this study, via the evaluation of relative performance of the four cases.

2. DATA AND METHOD

ROMS is a free-surface, hydrostatic ocean model solving primitive equations on topography-following-coordinates (Shchepetkin and McWilliams, 2003), which intends to provide multi-purpose oceanic simulation (e.g. Jiang et al., 2007; Liao et al., 2012; Wang et al., 2013). The governing equations of ROMS used in this study are 2D nonlinear shallow water (NSW) equations (Cushman-Roisin and Beckers, 2011). Although the NSW equations exclude dispersive effects, a previous study has shown that these effects are of less importance for the type of tsunami source in the 2011 Honshu earthquake (Grilli et al., 2012).

The continuity equation is:

$$\frac{\partial \eta}{\partial t}+\frac{\partial (Du)}{\partial x}+\frac{\partial (Dv)}{\partial y}=0 \tag{1}$$

The momentum equations in the Cartesian coordinates of x-direction and y-direction are:

$$\begin{aligned}&\frac{\partial (Du)}{\partial t}+\frac{\partial (Du^2)}{\partial x}+\frac{\partial (Duv)}{\partial y}-fDv\\&=-gD\frac{\partial \eta}{\partial x}+\frac{\partial}{\partial x}(DA_h\frac{\partial u}{\partial x})+\frac{\partial}{\partial y}(DA_h\frac{\partial u}{\partial y})-\tau_{xb}\end{aligned} \tag{2}$$

$$\begin{aligned}&\frac{\partial (Dv)}{\partial t}+\frac{\partial (Duv)}{\partial x}+\frac{\partial (Dv^2)}{\partial y}+fDu\\&=-gD\frac{\partial \eta}{\partial y}+\frac{\partial}{\partial x}(DA_h\frac{\partial v}{\partial x})+\frac{\partial}{\partial y}(DA_h\frac{\partial v}{\partial y})-\tau_{yb}\end{aligned} \tag{3}$$

in which η is the free surface; h is the depth of sea water under the average sea level; $D=h+\eta$, with D being the total depth of water column; u and v are the depth-integrated velocities in the eastward and northward directions; A_h is horizontal viscosity coefficient that is grid-size dependent with a maximum value of 600 m^2/s; and τ_b is the bottom stress with quadratic friction profile and a drag coefficient of 0.003. The fourth-order centered algorithm is used in the discretization of momentum equations.

The model domain extends from 56°S, 76°E to 68°N, 70°W, covering almost the whole Pacific Ocean with an orthogonal curvilinear coordinates (e.g. Chau and Jiang, 2004). The boundary of the 500×500 grids domain, with the "Arakawa C" type grids (Chau and Jiang, 2002), is outlined in Fig. 3 by a dashed line. The spatial resolution ranges from approximate 5 km near Japan to 100 km at the open boundary. The CFL condition constrains the time step of our grid set to less than 28 s, with maximum wave speed of ~300 m/s which is proportional to the square root of water depth; for the sake of temporal resolution we choose a time step of 12 s. Given the wavelength of tsunami wave in the order of tens to several hundred kilometers (Voit 1987), among all the computing nodes, ~67% of them will have more than 15 grids to discretize one wavelength of 300 km. But for far-field, the spatial resolution may be insufficient. Radiation open boundary condition is employed for free-surface at the southern boundary. Flather and Clamped boundary conditions are prescribed for the 2D velocity. The bottom topography is derived from the ETOPO2 database of the National Geophysical Data Center (NGDC).

The three earthquake sources used in this paper are seismic waveform analysis deformation. An earthquake source is a series of parameters, comprising dip angle, strike angle, rake angle, fault width, fault length, and fault depth that reproduce the features of an earthquake. We use the earthquake source data to calculate the deformation field via the Coulomb software (Lin, 2005; Toda et al., 2005), which is based on Okada's finite fault model. The deformation field includes both horizontal deformation (in eastward and northward direction) and vertical deformation (in upward direction). A total of four cases are considered. In Case 1, the deformation field uses the data of teleseismic P, SH, and long period surface waves with static GPS data from the California Institute of Technology (Caltech) (Wei and Sladen, 2011; Chen et al., 2012). In Case 2, it uses the data of teleseismic P, SH, and long period surface waves from the University of California at Santa Barbara (UCSB) (Shao et al. 2011). Case 3 uses similar data source as Case 2, except that the data is from the United States Geological Survey (USGS) (Hayes, 2012), In Cases 1 to 3, only the vertical deformation is considered, as the conventional tsunami genesis method. The vertical deformation field is used as the initial abnormal free-surface height field. The three initial deformation fields are summarized in Table 1 and displayed in Fig. 1. The main differences of the three source fields are the deformation area, fault depth and maximum deformation value. In Case 3, the fault center is shallower while the deformation region is smaller compared to Case 2 (see Table 1). The deformation ranges of the three source fields are -8.7-7.2 m, -1.8-9.6 m, and -3.4-7.0 m, respectively.

In order to improve the tsunami model, we also include the horizontal deformation in Case 4. The earthquake fault deformation is 3D, that it, in both vertical and horizontal directions. Conventional tsunami generation only takes vertical deformation into consideration. Voit (1987) reviewed the mechanism of momentum transfer in the horizontal direction via the impulsion by earthquake. Tanioka and Satake (1996) proposed the horizontal displacement would become significant when earthquake is taken place on steep slope. Song et al. (2008) considered the impulsion from the moving slope of horizontal deformation of earthquake, which contributed five times of the potential energy in the case of 2004 Sumatra-Andaman tsunami. In this paper, following the pioneered research we assume that the hydrodynamic model includes the initial kinetic energy besides the potential energy related to the vertical deformation. Analogous to the works of Wiegel et al. (1955) and Hu and Ye. (2006) on tsunami caused by submarine mass failure, the potential energy of the mass failure would be converted to the wave kinetic energy with a ratio of 1%. We consider a horizontal deformation generated initial velocity field, of which the kinetic energy (*KE*) is equal to 1% of the potential energy (*PE*) generated by the vertical deformation of Δh. The quantitative estimation of the converted ratio of 1% is shown in the Appendix. Then, we can write:

$$PE = \frac{1}{2} g\rho \iint_A |\Delta h|^2 dxdy \tag{4}$$

Table 1 Different sets of undersea earthquake data.

Case	Data source	Epicenter	Depth of fault (Km)	Strike angle (°)	Dip angle (°)	Range of deformation
Case 1	Lin Jian, WHOI	38.05° N, 142.8° E	24.0	201	9	136.0° ~ 149.0° E, 32.0° ~ 45.0° N
Case 2	Guangfu Shao, Xiangyu Li, et al., UCSB	38.10° N, 142.86° E	23.0	198	10	138.1° ~ 147.2° E, 32.7° ~ 43.1° N
Case 3	Gavin Hayes, USGS	38.32° N, 142.37° E	10.0	195	10	139.2° ~ 145.5° E, 35.3° ~ 41.3° N

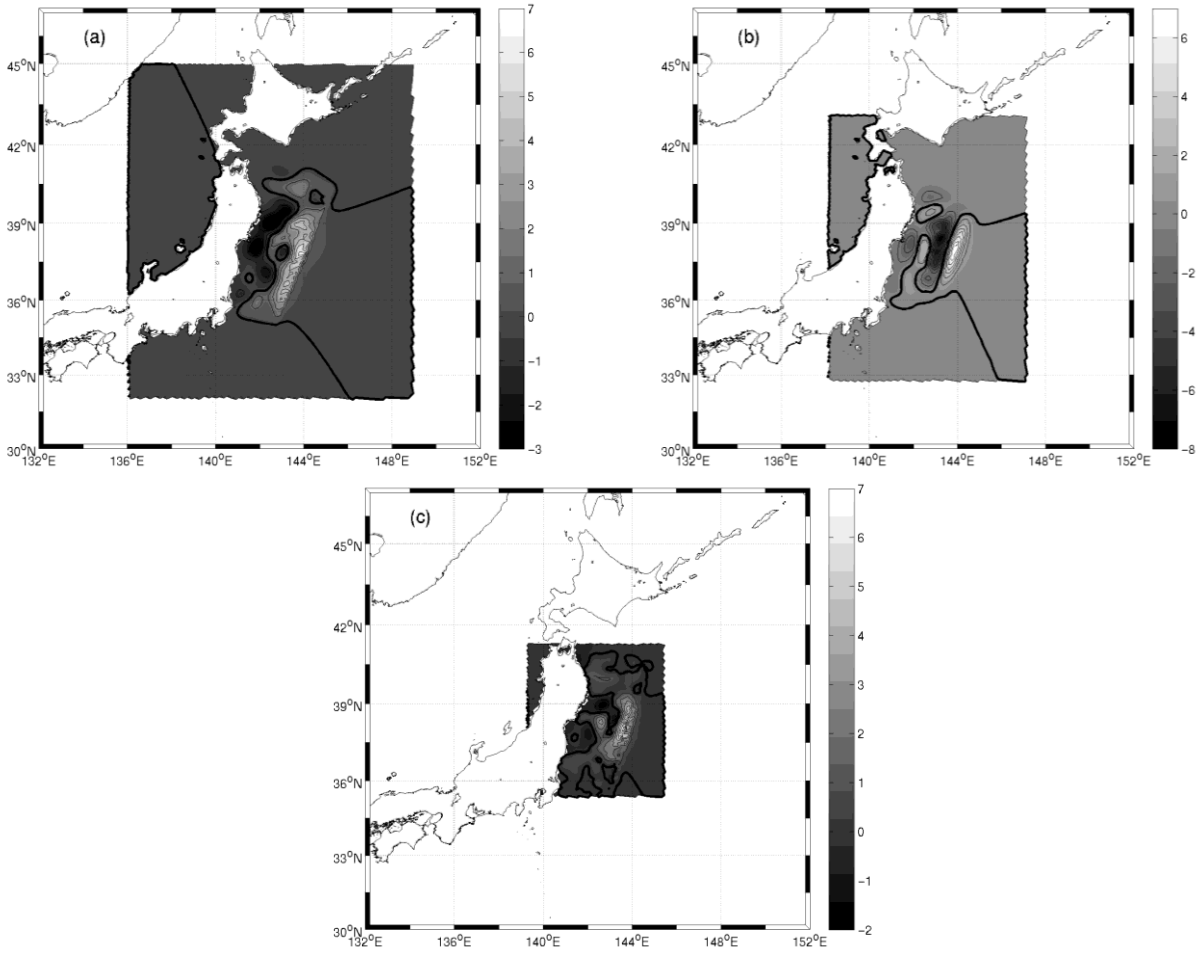

Fig. 1 Initial field of deformation (units: m) for earthquake of different sources: (a) Case 1, initial field from WHOI, (b) Case 2, initial field from UCSB and (c) Case 3, initial field from USGS. The thin contours are the isolines of deformation field with an interval of 1 m and the thick contour denotes zero deformation.

$$KE = \alpha PE = \frac{1}{2}\rho \iint_A (u^2 + v^2)dxdy \tag{5}$$

In the above equations, *PE* and *KE* are the accumulated potential and kinetic energy that are integrated over the deformation area. For each grid in the fault area, the initial *u*- and *v*-components of the horizontal velocity is proportional to the corresponding horizontal deformation:

$$(u, v) \propto (\Delta x, \Delta y) \tag{6}$$

Solving equations (4)-(6) will give us the velocity field as the initial condition of the hydrodynamic model. The initial horizontal velocity field generated by this method is shown in Fig. 2.

The model results are validated using the real-time observation record of the Deep-ocean Assessment and Reporting of Tsunami (DART) buoys maintained by the National Data Buoy Center of NOAA (Gonzalez et al., 1998; also see http://www.ndbc.noaa.gov/dart.shtml). The DART buoy data is the earliest direct measure of tsunami wave, with high signal-to-noise ratio

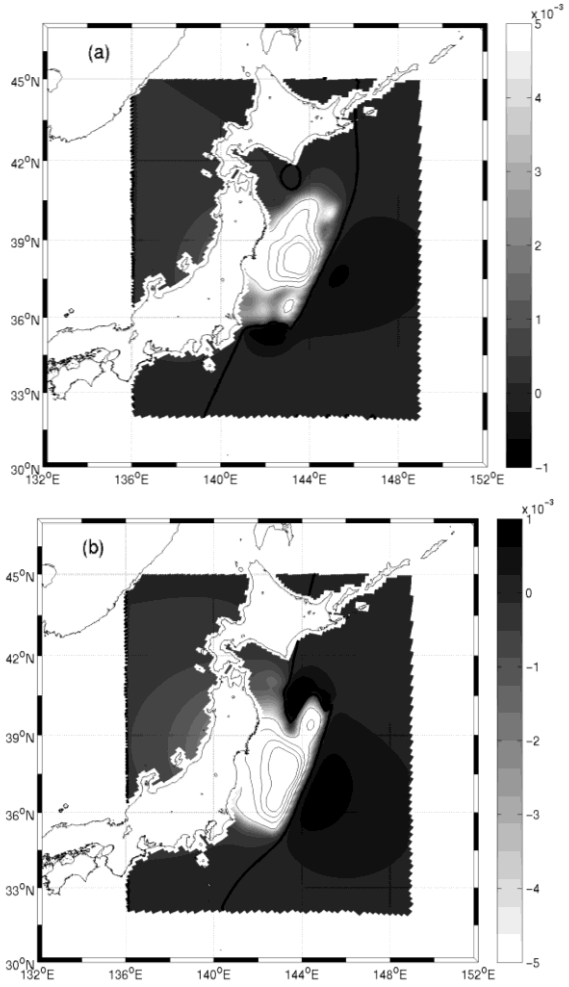

Fig. 2 Velocity pattern caused by horizontal deformation in initial field: (a) u component, positive value for eastward, and (b) v component, positive value for northward. The contour interval is $5*10^{-3}$ m/s. and the thick contour denotes the zero contour.

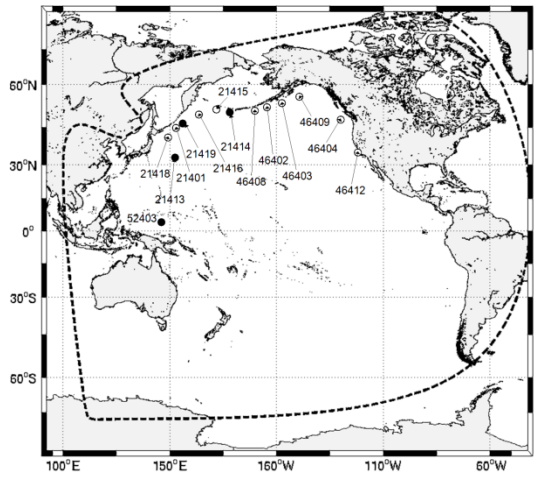

Fig. 3 Locations of DART buoy stations. The tsunami wave time series at Stations 21414, 21413, 21419 and 52403 (solid dots) are used to validate the modeled results. The dashed line indicates the computing domain.

compared to tide gage data (Tang et al., 2009). The observation record is low-pass filtered to isolate the low-frequency component. The locations of the buoys are shown in Fig. 3. We choose 14 DART buoys (Fig. 3; indexed by solid and hollow dots) to validate the maximum wave amplitude from the model. In particular, we use four of the buoys (in hollow dots) to validate the time series of tsunami wave.

3. RESULTS AND DISCUSSION

In this section, we validate and evaluate the model performance in the four cases using Figs. 4-8. The modeled maximum wave amplitudes during first 24 hrs in Cases 1-3 are shown in Figs. 4a to 4c. The amplitude of Case 4 is almost the same as that in Case 1, so it is not shown. For comparison, the model result by NOAA is shown in Fig. 4d. The square of the tsunami wave amplitude in the deep sea is simply proportional to the energy of the tsunami wave according to the theory of shallow-water gravity wave; therefore, Fig. 4 also shows the tsunami wave energy distribution. It shows that the propagations of tsunami in the three cases are similar. The propagation of tsunami is affected by two main factors: the focusing configuration of the source region and the waveguide structure of mid-ocean ridges (Titov et al., 2005). In the near-field region, i.e., the northwestern Pacific Ocean, the extension of the earthquake source region determines the wave propagation pattern. Because of a smaller deformation region, the tsunami wave in Case 3 propagates offshore with a higher amplitude, while the wave in Case 2 is stronger in the alongshore direction and weaker in the offshore direction. In the far-field, the bottom topography plays an important role in tsunami propagation. For example, around the Hawaiian Islands and along the ridge, the convergent boundaries of Nazca plate and Antarctica plate, the maximum wave amplitude from Hawaii to Chile is obviously higher than the surrounding due to shallow-water effect. The ocean ridge acts as a waveguide and determines the direction of propagation. The tsunami wave in Case 3 propagates alongshore more significantly than that in the other cases; this weakens the offshore propagation. The propagation pattern in Case 1 agrees best with NOAA's tsunami wave forecast (Fig. 4d).

Fig. 5 shows the arrival times of the first tsunami wave in the four cases. In all cases, it takes about 18 hrs for the simulated wave to propagate across the Pacific to reach the coast of Chile. The arrival

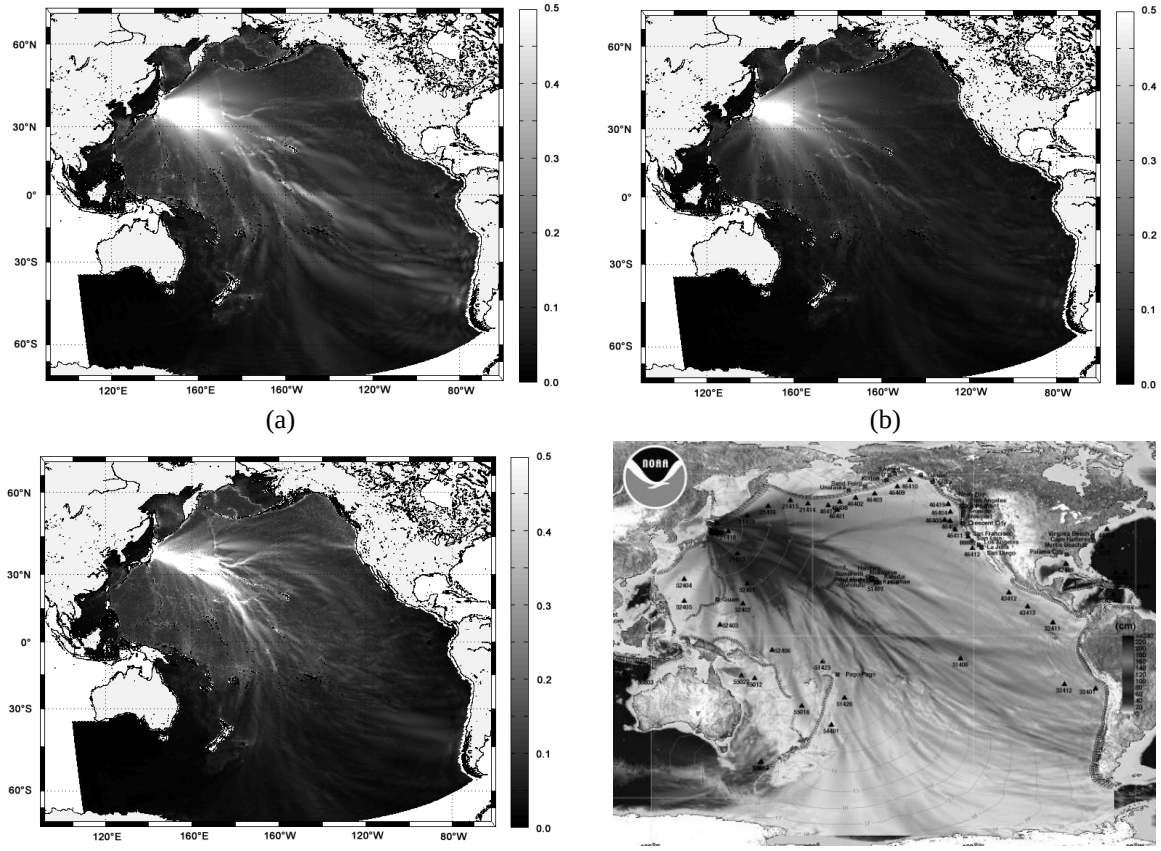

Fig. 4 Modeled maximum tsunami wave amplitude (units: m) during first 24 hours in the three cases of (a) Case 1, (b) Case 2, and (c) Case 3, and (d) model result from PMEL/NOAA (http://nctr.pmel.noaa.gov/honshu 20110311/).

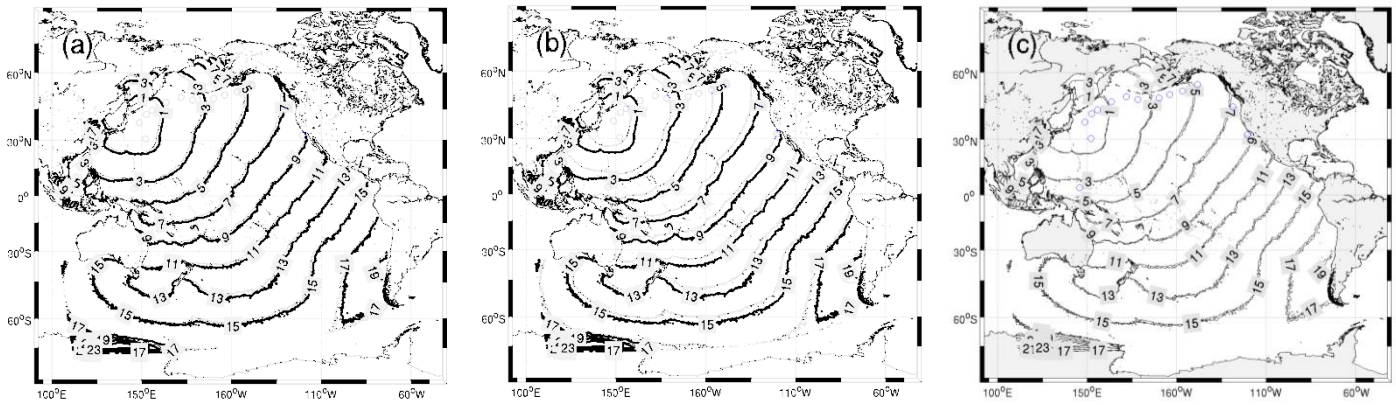

Fig. 5 Modeled arrival times (thin contours; units: hour) of first tsunami-wave elevations in (a) Case 2 and (b) Case 3, superimposed on that of Case 1 (bold contours). (c) Arrival times in Case 4 (the "faster" contours) and Case 1. Hollow dots are the 14 DART buoy stations first shown in Fig. 3.

times in the four cases show very small differences, especially for the far-field propagation, while all simulated waves present time shifts toward earlier arrivals. For tsunami propagation models, time discrepancy (i.e., numerically tsunami travels faster by 2-3%) is common, which may be resulted from the excluded effect of elasticity and self-gravity of the Earth (Watada et al., 2012). In Case 1, modeled tsunami wave propagates southwestward faster than those in Case 2 and Case 3. Arrival time in Case 3 is several minutes later than those in Cases 1 and 2, which may be caused by the smallest deformation region among the three cases. On the other hand, comparing the arrival time of the first wave peak with the data from the DART stations except for Station 46412 (which is located near the western coast of the US; see Fig. 3), the errors

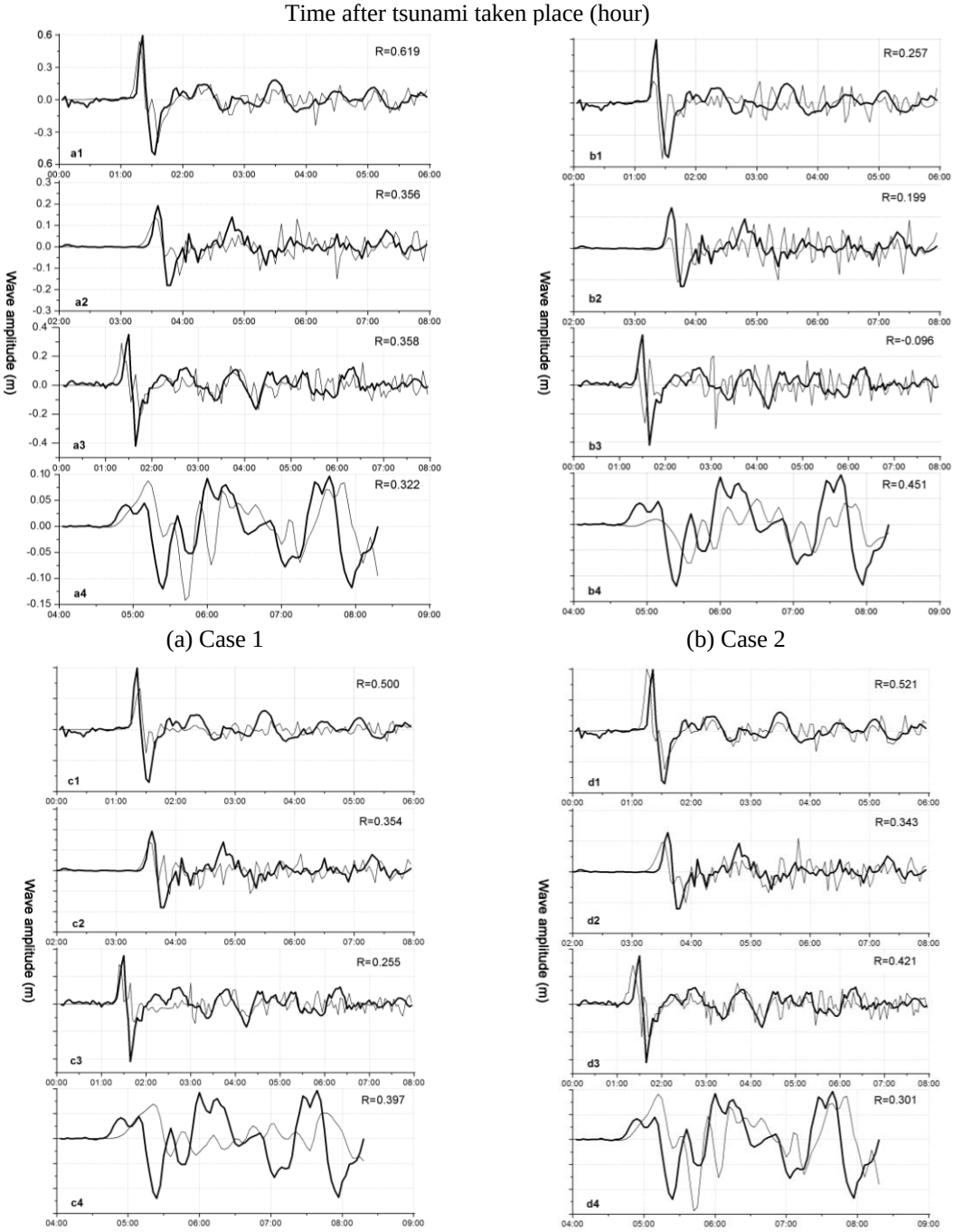

Fig. 6 Modeled (thin lines) and observed (bold lines) tsunami time series at DART buoys Stations 21413 (a1, b1, c1, d1), 21414 (a2, b2, c2, d2), 21419 (a3, b3, c3, d3), and 52403 (a4, b4, c4, d4). In each panel, the correlation coefficient (R) is shown near its upper right corner.

of arrival time at the other 13 stations are averaged at 2.82 min (relatively 2.36%, in Case 1), 2.28 min (relatively 1.79%, in Case 2), 3.48 min (relatively 2.27%, in Case 3), and 3.72 min (3.92% in Case 4) earlier than in observation. At Station 46412, the errors are as high as ~3 hr, which are -24.3%, -23.6%, 25.0%, and 25.1% in the four cases, respectively. The reason may be the lower grid resolution (only ~100 km) near the station; as a result, the bottom topography of the US west coast cannot be represented well in the model, as the water depth determines the speed of shallow-water wave. The error of arrival time of first wave peak increases from 2.4 min in Case 4 to 3.6 min in Case 1, all earlier compared to the observation at the 13 DART stations (excluding Station 46412).

Fig. 6 shows the modeled and observed tsunami time series at the DART buoy Stations 21413, 21414, 21419, and 52403. In each panel, the

correlation coefficient (R) between observation and simulation at each station is also presented. We can see that the model result of Case 1 agrees well with the observation in terms of tsunami wave evolution and wave height. For the first several waves, good agreement is obtained at Station 21413 in Case 1 (Fig. 6, a1). The correlation between Case 2 result and observation is comparatively the lowest of the four cases, underestimating the wave height (Fig. 6, b1-b4) while reasonably reproducing the first trough of the tsunami wave (Fig. 6, b1-b3). Compared to Case 2, Case 3 is better in terms of simulated maximum wave amplitude. The correlation coefficient in Case 4 (Fig. 6d) of wave time series indicates that the simulation of tsunami wave evolution does not improve. DART Station 21413 is the closest buoy to the epic center and has much higher tsunami wave height; therefore, its correlation coefficients are the highest among all the buoys', which are 0.619 (Case 1), 0.500 (Case 3), and 0.521 (Case 4), except for Case 2 (in which the highest R squared occurs at Station 52403). Poor correlation is seen at Station 21419, especially in Case 2, which did not reproduce the first peak of wave but generated several following peaks. The sensitivity experiments of Tang et al. (2009) showed that inaccurate topography can produce poor or incorrect simulation results. The uncertainty of the simulations is primarily attributed to the coarse model grid resolution and uncertainty of tsunami source field. In this study, the spatial resolution is not high enough to reflect the sea surface fluctuation of one single station, especially in the far-field region. For a grid with a relatively lower spatial resolution, about 100 km at the far-field, the error of wave height is higher although the computing time reduced significantly. To obtain a better simulation result, the increase of the spatial resolution of the grid would be an effective way. For the near-shore simulation, 2D shallow-water assumption without dispersive effect could also be a limitation.

Fig. 7 displays the errors of maximum wave amplitude between model results and observation from all 14 DART buoys stations. Table 2 includes the statistical errors of the four cases. The average errors are 23.2% (Case 1), 37.4% (Case 2), 26.9% (Case 3), and 20.6% (Case 4), compared with all 14 observations. All the cases underestimate the maximum wave amplitude. When observed wave amplitude is less than 0.3 m, the error is 0.034 m (23.7% relatively in Case 1), 0.033 m (31.6% relatively in Case 2), 0.035 m (26.3%, in Case 3), and 0.028 m (22.0%, in Case 4). At these buoy stations, the noises of

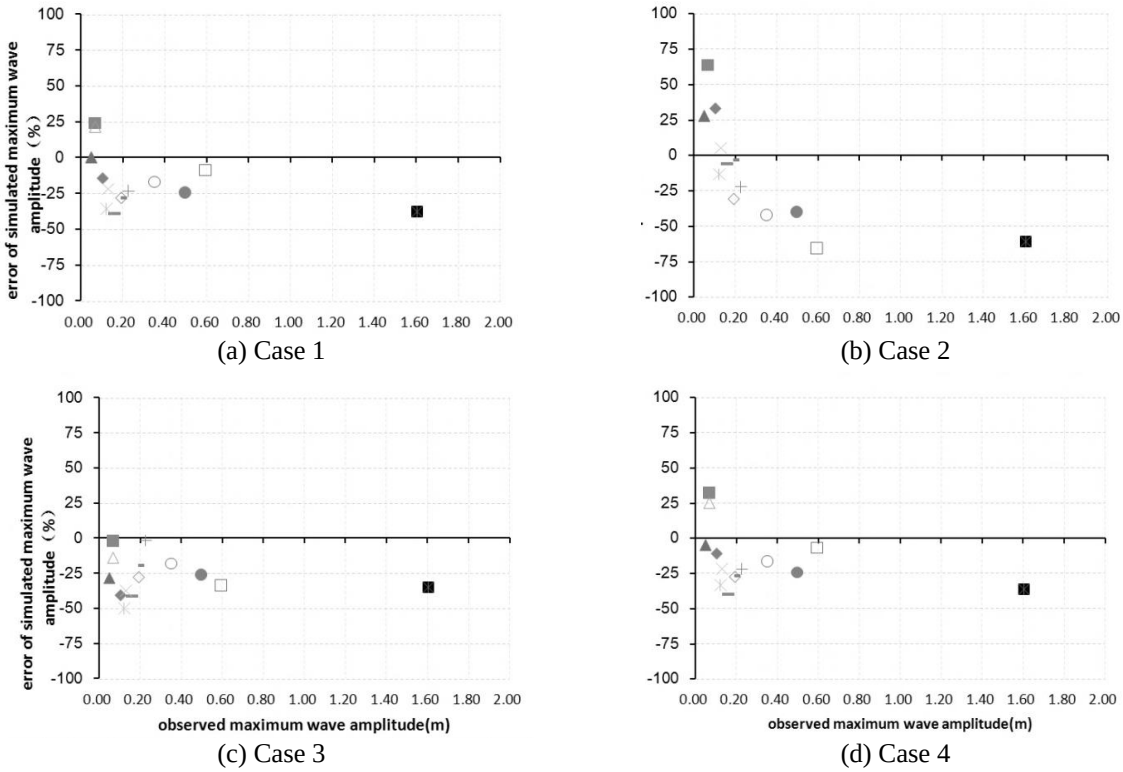

Fig. 7 Errors of maximum wave amplitude between model results and observations from 14 DART buoys stations. Model error is defined by $(H\text{-}H_o)/H_o$, where H is modeled maximum wave amplitude and H_o is the observed maximum wave amplitude at a DART station. For Station 46409 in Case 2, the error is greater than 100% (therefore not seen in the plot).

Table 2 Errors of modeled maximum tsunami wave amplitude in four cases.

		Case 1	Case 2	Case 3	Case 4
When H_0 > 0.3 m [b]	Absolute (units: m)	0.210	0.427	0.239	0.150
	Relative (%) [a]	22.1	51.9	28.2	17.2
When H_0 < 0.3 m	Absolute (units: m)	0.034	0.033	0.035	0.028
	Relative (%) [a]	23.7	31.6	26.3	22.0
All observations at 14 stations	Absolute (units: m)	0.085	0.145	0.093	0.062
	Relative (%) [a]	23.2	37.4	26.9	20.6
RMSE (units: m) [c]		0.029	0.084	0.028	0.014

[a] Relative error is defined by $|(H-H_o)|/H_o$, where H and H_o are modeled and observed maximum wave amplitude at each DART station, respectively.

[b] Include DART Stations 21401, 21413, 21418, and 21419, which have H_0>0.3 m.

[c] Root Mean Squared Error (RMSE) is defined as $\sqrt{\frac{\sum_{1}^{n}(H-H_o)^2}{n}}$, n =14.

instrument and numerical errors are the sources of errors. When the observed amplitude is greater, the absolute errors are greater (see Table 2). The relative error of Case 1 is 22.1% when the observed amplitude is greater than 0.3 m. Fig. 7c shows the relative errors of Case 3 are no greater than 50%, underrating the wave amplitude at all buoy stations. The errors in Case 2 are less than ±65% at the 13 stations (excluding Station 46409), which are obviously greater than those in Case 1 and Case 3. The RMSEs in the four cases are 0.029, 0.084, 0.028, and 0.014 m, respectively. The average error of maximum wave amplitude at the 14 DART stations is reduced from 23.2% in Case 1 to 20.6% in Case 4 (see Table 1). When observed wave height is greater than 0.3 m, the error is reduced from 22.1% in Case 1 to 17.2% in Case 4. These results indicate that with horizontal deformation (as in Case 4) the model performance is improved in terms of maximum tsunami wave amplitude.

Fig. 8 displays the Taylor's diagram (Taylor, 2001) that summarizes the model performance of maximum wave amplitude in the four cases. When considering all 14 stations, all correlation coefficients are greater than 0.97 and all of the normalized standard deviations (NSDs) are between 0.3 and 0.8, indicating that all the cases tend to underrate the amplitude of tsunami wave. In each case, when restricted by the observed amplitude to be greater than 0.3 m, the simulation performance is better (where the NSDs are approximately 0.1~0.2 higher) than that when the observed amplitude is below 0.3 m. The performances of Case 1 and Case 3 are comparable, though Case 3 is slightly closer to the observations in terms of NSD. Compared with

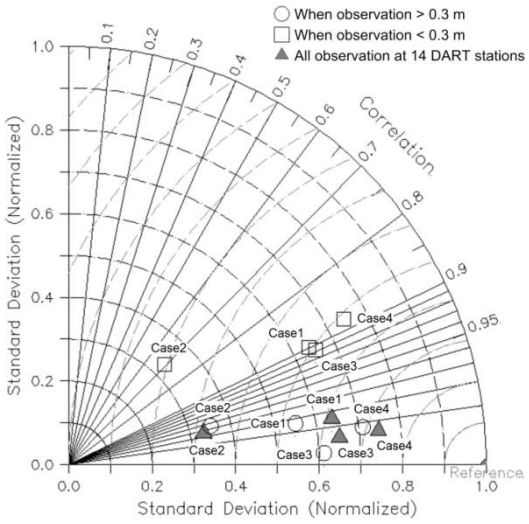

Fig. 8 Taylor diagram comparing maximum wave amplitude simulations in the four cases summarized at all 14 observation stations in filled triangles. The comparisons are also divided into two groups: amplitude greater than 0.3 m in open circles at DART Stations 21401, 21413, 21418, and 21419; and amplitude smaller than 0.3 m in open squares at the rest of the DART stations. The radial distance from 0.0 to 1.0 is the normalized standard deviation. The azimuthal position is the correlation coefficient (R). The distance between an individual point and the "reference" point shows the normalized RMSE. The value used for the normalization is the standard deviation of the observed wave amplitude, σ_{obs}.

the other cases, Case 3 has relatively higher correlations, which are 0.995 (all stations), 0.999 (amplitude >0.3 m), and 0.907 (amplitude <0.3 m), indicating that the maximum wave pattern agrees well with the observation. Case 4 also has

relatively high correlation coefficients. On the other hand, the RMSEs of the four cases are 0.029, 0.028, 0084, and 0.014 (for all buoy observations), respectively. In summary, although the inclusion of vertical velocity worsens the error of arrival time, Case 4 is still relatively higher in terms of correlation and best in terms of the normalized RMSE. Above all, the consideration of horizontal energy input in Case 4 increases the simulation accuracy of maximum wave amplitude.

The methodology used in this study has several limitations. First, 2D NSW model limited the fully resolving of the wave processes, especially the near shore processes interacting with the bottom topography. Employment of 3D model with fully dispersive effect (Tappin et al., 2001; Zhang et al., 2010), realistic forcing conditions (Chen et al., 2012) and more sophisticated topography would be a better approach. Second limit is the limitation of spatial resolution of computing domain. For higher efficiency the spatial resolution is sacrificed, even though orthogonal curvilinear grid partially compensated the limitation. With multilevel two-way nested grids (e.g. Tang et al., 2009; Yamazaki et al., 2012), this limitation would be broken through; nevertheless, the two-way nested version of ROMS is currently not available. The nested model would be considered in the further simulation of tsunami wave. Third, the initial conditions in all cases are instantaneous disturbances of sea surface, while the earthquake is a time-dependent process releasing energy within ~200s.

4. CONCLUSIONS

Accurate simulation of tsunami wave in terms of wave amplitude and arrival time is very important to tsunami forecast and warning. In this paper, different tsunami source deformation fields are used to simulate the propagation of the tsunami that took place near Honshu, Japan on 11 March 2011. We compare the effects of different earthquake deformations on the tsunami simulation, which provides us a better understanding of earthquake-induced tsunami's generation and propagation processes.

Four cases driven by different deformation fields reproduce the tsunami waves reasonably, although the energy of tsunami waves is underestimated in general. The validation in terms of wave pattern, arrival time and maximum wave amplitude indicates that Case 1 gives the best estimation than Case 2 and Case 3. The spatial resolution of grid limited the simulation, as well as the assumption of 2D shallow-water equation. The application of two-way nested grid in the ROMS is currently not available, which is thought to be able to improve the simulation efficiency and near-shore resolution.

When the horizontal deformation, of which the corresponding initial kinetic energy equaled to 1% of the potential energy, was taken into account in Case 4, the model performance was improved by about 3% in terms of maximum tsunami wave amplitude; and the RMSE was reduced from 0.029 to 0.014 m. In Case 4, although arrival time error increased compared with Case 1, but (3.72 min) 3.9% error is still in reasonable range. Nonetheless, the more accurate simulation of maximum wave amplitude offered a closer assessment of tsunami hazard, which is important in the forecast of tsunami wave. These results show that the horizontal energy of earthquake deformation should be included to improve the performance of tsunami simulation, but the exact mechanism of the horizontal displacement on the genesis of earthquake tsunamis needs further examination.

ACKNOWLEDGEMENTS

This work was supported by grant (2010121029) from the Fundamental Research Funds for the Central Universities, and the National Key Technology R&D Program (2013BAB04B00). We thank NOAA's Pacific Marine Environmental Laboratory (PMEL) and Center for Tsunami Research (CTR) for providing their tsunami research results. More detail can be found at http://nctr.pmel.noaa.gov/honshu20110311.

REFERENCES

1. Avouac JP (2011). Earthquakes: The lessons of Tohoku-Oki. *Nature* 475(7356):300-300.
2. Chau KW, Jiang YW (2002). Three-dimensional pollutant transport model for the Pearl River Estuary. *Water Research* 36(8):2029-2039.
3. Chau KW, Jiang YW (2004). A three-dimensional pollutant transport model in orthogonal curvilinear and sigma coordinate system for Pearl River estuary. *International Journal of Environment and Pollution* 21(2):188-198.
4. Chawla A, Kirby JT (2000). A source function method for generation of waves on

currents in Boussinesq models. *Applied Ocean Research* 22:75-83.
5. Chen CS, Lai ZG, Beardsley RC, Sasaki J, Lin J, Lin HC, Ji R (2012). The March 11, 2011 Tohoku M9.0 earthquake-induced tsunami and coastal inundation along the Japanese coast: A model assessment. *Journal of Geophysical Research* (In press).
6. Cushman-Roisin B, Beckers JM (2011). *Introduction to Geophysical Fluid Dynamics: Physical and Numerical Aspects*. Academic Press.
7. González FI, Milburn HM, Bernard EN, Newman J (1998). Deep-ocean Assessment and Reporting of Tsunamis (DART): brief overview and status report. *Proceedings of the Inter-national Workshop on Tsunami Disaster Mitigation*. Available at: http://www.ndbc.noaa.gov/dart/brief.shtml.
8. Grilli ST, Harris JC, Bakhsh TST, Masterlark TL, Kyriakopoulos C, Kirby JT, Shi FY (2012). Numerical simulation of the 2011 Tohoku tsunami based on a new transient FEM co-seismic source: Comparison to far- and near-field observations. *Pure and Applied Geophysics*.
9. Hayes G (2012). Available at: http://earthquake.usgs.gov/earthquakes/eqinthenews/2011/usc0001xgp/finite_fault.php.
10. Hu TJ, Ye YC (2006). Prediction models of landslide tsunami and its application. *Journal of Marine Sciences* 24(3):21-31 (In Chinese).
11. Jiang Y, Zhang X, Hong H, Chi T (2007). Ocean observing data web service and application in shipwreck salvation of Taiwan Strait. *IEEE Wireless Communications, Networking and Mobile Computing International Conference*, 5819-5822.
12. Kilinc I, Hayir A, Cigizoglu HK (2009). Wave dispersion study for tsunami propagation in the Sea of Marmara. *Coastal Engineering* 56:982-991.
13. Kowalik Z, Proshutinsky A (2010). Tsunami–tide interactions: A Cook Inlet case study. *Continental Shelf Research* 30:633-642.
14. Liao EH, Jiang YW, Li L, Hong HS, Yan XH (2013). The cause of the 2008 cold disaster in the Taiwan Strait. *Ocean Modelling* 62:1-10.
15. Lin J, Stein RS (2004). Stress triggering in thrust and subduction earthquakes, and stress interaction between the southern San Andreas and nearby thrust and strike-slip faults. *Journal of Geophysical Research* 109:B02303.
16. Mellor GL, Yamada T (1982). Development of a turbulence closure model for geophysical fluid problems. *Reviews of Geophysics and Space Physics* 20(4):851-875.
17. Okada Y (1985). Surface deformation due to shear and tensile faults in a half space. *Bulletin of the Seismological Society of America* 75:1135-1154.
18. Olabarrieta M, Medina R, Gonzalez M, Otero L (2010). C3: A finite volume-finite difference hybrid model for tsunami propagation and runup. *Computers and Geosciences* 9:1-12.
19. Satake K (1995). Linear and nonlinear computations of the 1992 Nicaragua earthquake tsunami. *Tsunamis: 1992–1994*. Springer.
20. Shao G, Li X, Ji C, Maeda T (2011). Focal mechanism and slip history of 2011 Mw 9.1 off the Pacific coast of Tohoku earthquake, constrained with teleseismic body and surface waves. *Earth Planets Space* 63(7):559-564.
21. Shchepetkin AF, McWilliams JC (2003). The regional ocean modeling system: A split-explicit, free-surface, topography-following-coordinate ocean model. *Ocean Modeling* 9:347-404.
22. Song YT, Fu LL, Zotnicki V, Ji C, Hjorleifsdottir V (2008). The role of horizontal impulses of the faulting continental slope in generating the 26 December 2004 tsunami. *Ocean Modeling* 20:362-379.
23. Tanioka Y. Satake K. (1996). Tsunami generation by horizontal displacement of ocean bottom. *Geophysical Research Letters* 23:861-864.
24. Tang L, Titov VV, Chamberlin CD (2009). Development, testing, and applications of site-specific tsunami inundation models for real-time forecasting. *Journal of Geophysical Research* 114:1-22.
25. Tappin DR, Watts P, McMurtry G.M, Lafoy Y (2001). The Sissano, Papua New Guinea tsunami of July 1998-offshore evidence on the source mechanism. *Marine Geology* 175:1-23.
26. Taylor KE (2001). Summarizing multiple aspects of model performance in a single diagram. *Journal of Geophysical Research* 106(D7):7183-7192.
27. Titov V, Rabinovich AB, Mofjeld HO, Thomson RE (2005). The global reach of the 26 December 2004 Sumatra tsunami. *Science* 309(23):2045-2048.
28. Toda S, Stein RS, Richards-Dinger K, Bozkurt S (2005). Forecasting the evolution of seismicity in southern California: Animations built on earthquake stress

transfer. *Journal of Geophysical Research* B05S16.
29. Voit SS (1987). Tsunamis. *Annual Review of Fluid Mechanics* 19:217-236.
30. Wang J, Hong HS, Jiang YW, Chai F, Yan XH (2013). Summer nitrogenous nutrient transport and its fate in the Taiwan Strait: a coupled physical-biological modeling approach. *Journal of Geophysical Research* (Accepted).
31. Watada S, Satake K, Fujii Y (2012). Origin of travel time anomaies of distant tsunami. In: *AGU Fall Meeting 2011 poster NH11A*.
32. Wei S, Sladen A (2011).Tohoku earthquake source model, preliminary result. Available at: http://tectonics.caltech.edu/slip_history /2011_tohoku-oki-tele/index.html.
33. Wen RZ, Ren YF, Li XJ (2011). The tsunami simulation for off the Pacific coast of Tohoku earthquake and disaster mitigation in China. *Journal of Earthquake Engineering and Engineering Vibration* 4:23-27 (In Chinese).
34. Wiegel RI (1955). Laboratory studies of gravity waves generated by movement of a submarine body. *Transactions of American Geophysical Union* 36(5):759-774.
35. Yamazaki Y, Lay T, Cheung KF, Yue H, Kanamori H (2011). Modeling near-field tsunami observations to improve finite-fault slip models for the 11 March 2011 Tohoku earthquake. *Geophysical Research Letter* L00G15.
36. Yamazaki Y, Cheung KF, Pawlak G, Lay T (2012). Surges along the Honolulu coast from the 2011 Tohoku tsunami. *Geophysical Research Letter* L09604.
37. Zhang HS, Wang WY, Feng WJ, Wang YL, Yang JM (2010). Test and applications of a Boussinesq model with ambient current. *Journal of Hydrodynamics* 22(4):526-536.

APPENDIX: ESTIMATION OF CONVERT RATIO α

In the conventional vertically-forced tsunami generation theory, Okada's deformation is applied as sea surface displacement instantaneously. On the other hand, the horizontal deformation of tsunami gives an impulse to the sea water in horizontal direction, which will also contribute to the tsunami wave (Song et al., 2008). In the frame of 2D model, one is not able to figure out the exact impulsion processes which are 3 dimensional. Instead of resolving the 3D process, we use an energetic estimation to represent the contribution of horizontal deformation (i.e. driving via initial velocity). Following Tanioka and Satake (1996) and Song et al. (2008), we assume that (Δx, Δy, Δz) are the earthquake faults displacements in the eastward, northward, and upward directions, and the total vertical deformation Δh can be written as:

$$\Delta h = h_{vertical} + h_{horizontal} = \Delta z + \Delta x \cdot \frac{\partial h}{\partial x} + \Delta y \cdot \frac{\partial h}{\partial y} \tag{7}$$

where h is bottom topography, the horizontal component of Δh is proportional to the horizontal displacement and the water depth gradient in the corresponding direction. In the instance of Case 1, the ratio α, accumulated *PE* of $h_{horizontal}$ to that of $h_{vertical}$ is:

$$\alpha = \frac{\iint_A \left(\Delta x \cdot \frac{\partial h}{\partial x} + \Delta y \cdot \frac{\partial h}{\partial y} \right)^2 dxdy}{\iint_A (\Delta z)^2 dxdy} = 0.0102 \approx 1\% \tag{8}$$

This ratio indicates the energy of horizontal deformation is about 1% to that of vertical deformation of earthquake in Case 1. On the other hand, we consider that horizontal deformation drives the overlying water column with an instantaneous impulsion, via which the *KE* would have the same order as $h_{horizontal}$. To give an impulse to the water column respectively in the *x*- and *y*- directions, instead of simply adding on a horizontal component of Δh, we choose the horizontal velocity as the modified theory to generate tsunami wave as described in Section 2 with a convertion ratio of 1%.